Materials Science & Engineering B 236–237 (2018) 179–188

Contents lists available at ScienceDirect

Materials Science & Engineering B

journal homepage: www.elsevier.com/locate/mseb

# Electrical transport properties and complex impedance investigation of $Fe^{3+}$ and $La^{3+}$ co-doping (Pb,Sr)$TiO_3$ thin films

F.M. Pontes[a,*], D.S.L. Pontes[a], A.J. Chiquito[b], Y.N. Colmenares[c], V.R. Mastelaro[c], E. Longo[a,d]

[a] Department of Chemistry, Universidade Estadual Paulista – Unesp, P.O. Box 473, 17033-360 Bauru, São Paulo, Brazil
[b] NanO LaB – Department of Physics, Universidade Federal de São Carlos, Via Washington Luiz, Km 235, P.O. Box 676, 13565-905 São Carlos, São Paulo, Brazil
[c] Physics Institute of São Carlos (IFSC), Universidade de São Paulo, São Carlos, SP, Brazil
[d] LIEC – CDMF – Department of Chemistry, Universidade Federal de São Carlos, Via Washington Luiz, Km 235, P.O. Box 676, 13565-905 São Carlos, São Paulo, Brazil

ARTICLE INFO

*Keywords:*
Impedance spectroscopy
Dielectric relaxation
Electrical transport
Thin films

ABSTRACT

This work investigates the impact of $Fe^{3+}$ and $La^{3+}$ co-doping on the structural, electrical transport and dielectric relaxation properties of PST thin films. XRD and Raman spectroscopy data show that the $Fe^{3+}$ and $La^{3+}$ doping induce a pseudocubic to tetragonal structural phase transformation. Schottky barrier heights calculated from temperature-dependent current–voltage plots for the PST, PSTF and PSLTF films decreased to 1.20, 0.59, and 0.36 eV, respectively. This behavior was directly assigned to the increase in oxygen vacancies. The frequency dependence of sample's impedance revealed the presence of the typical electrical relaxation phenomenon in all films. Activation energies calculated from the imaginary part of the impedance are 1.73 and 0.57 eV: the high value (1.73 eV, PST films) suggests the presence of long-range oxygen vacancy diffusion, while the lower one (0.57 eV PSLTF films) should be associated to the short-range oxygen vacancy diffusion.

## 1. Introduction

Many perovskite thin films materials have been studied to explore the fascinating physics properties which include ferroelectric, dielectric, intelligent sensor, photovoltaic and solid oxide fuel cells [1–4]. The ability to tune the physical properties of perovskite thin films materials are mainly attributed to deposition parameters, types and location in the crystal lattice of substitution atoms (doping). Nowadays, most of perovskite thin films materials are not simple compounds as at the beginning of the twentieth century, e.g., $BaTiO_3$, $SrTiO_3$, $BiFeO_3$, $PbTiO_3$ [5–8] but rather complex compounds. Perovskite thin films materials with two or more different atoms either isovalent or heterovalent in A- and B- sublattice of perovskite are examples of these new and complex compounds [9,10]. In this way, Leung et al. reported on the electrical and magnetic properties of $La_{0.35}Sr_{0.65}Ti_{1-x}Fe_xO_3$ perovskite thin films [11]. Wang et al. have reported that the Bi doping have a significant effect on the dielectric and ferroelectric properties of $[Pb_{0.95}(La_{1-y}Bi_y)_{0.05}][Zr_{0.53}Ti_{0.47}])O_3$ thin films [12]. As reported by Liu et al. addition of a small amount of Mn effectively reduces the dielectric loss of the $0.63Bi(Mg_{1/2}Ti_{1/2})O_3$–$0.37PbTiO_3$(BMT–0.37PT–xMn, x = 0–0.01) thin films [13]. Recently, Kumar et al. report the synthesis of single-phase $Pb(Fe_{0.66}W_{0.33})_{0.80}Ti_{0.20}O_3$ thin films by chemical solution deposition on Pt/Ti/$SiO_2$/Si (1 0 0) substrates which displayed weak ferromagnetic properties [14].

However, when combining different ions into the A and/or B sublattices is very common the formation of point defects such as oxygen vacancies, cation vacancies and complex dipole defects [15–17]. The presence of point defects is considered to be the main cause of different relaxation processes, which are characterized by different energy barriers. Hence the development of complex perovskite thin films for high performance devices is a serious issue in technology nowadays. For instance, Li et al. demonstrated that oxygen vacancies are the origin of the dielectric relaxation behavior in $(BaTiO)_{1-x}$:$(Sm_2O_3)_x$ thin films [18]. Ke et al. have investigated the electrical conduction behavior in $Bi_{0.9}La_{0.1}Fe_{0.98}Mg_{0.02}O_3$ ferroelectric thin films [19]. In addition, Lahmar et al. have reported a study on leakage current mechanism and relaxation behavior of $BiFeO_3$–$LaMnO_3$ $[Bi_{1-x}La_xFe_{1-x}Mn_xO_3$ $(0 \le x \le 0.1)]$ thin films [20]. Temperature-dependent complex impedance analysis of $Bi_{3.15}Nd_{0.85}Ti_{2.99}Mn_{0.01}O_{12}$ ferroelectric thin films have been conducted by Zhang et al [21]. They have proposed a model in which improved fatigue endurance is due to the lower density of oxygen vacancies.

The present investigation reports in detail the effects of $Fe^{3+}$ and $La^{3+}$ addition on electrical conduction behavior of $Pb_{0.70}Sr_{1-x}La_xTi_{1-y}Fe_yO_3$ thin films. The complex impedance analysis showed a dielectric relaxation process and it seems to be intimately associated to the incorporation of Fe and La ions into the A- and B-site sublattices.

* Corresponding author.
*E-mail address:* fenelon@fc.unesp.br (F.M. Pontes).

https://doi.org/10.1016/j.mseb.2018.11.013
Received 14 November 2017; Received in revised form 7 November 2018; Accepted 25 November 2018
Available online 29 November 2018
0921-5107/ © 2018 Elsevier B.V. All rights reserved.

## 2. Experimental procedure

$Pb_{0.70}Sr_{0.30}TiO_3$ (PST), $Pb_{0.70}Sr_{0.30}Ti_{1-x}Fe_xO_3$ (x = 0.50) (PSTF) and $Pb_{0.70}Sr_{0.30-x}La_xTi_{1-y}Fe_yO_3$ (x = 0.10 and y = 0.50) (PSLTF) thin films were deposited on Pt/Ti/$SiO_2$/Si substrate by chemical solution deposition. The precursor solution for the PST, PSTF and PSLTF were prepared by the well-known polymeric precursor route using strontium acetate $Sr(CH_3COO)_2$, lanthanum acetate $La(CH_3COO)_2$, titanium isopropoxide $Ti(C_{16}H_{28}O_6)$, lead acetate trihydrate $[Pb(CH_3CO_2)_2{\cdot}3H_2O]$, iron nitrate $[Fe(NO_3)_3{\cdot}9H_2O]$, ethylene glycol ($CH_2OHCH_2OH$), and deionized water ($H_2O$) as solvent. Details of the preparation method can be found in the literature [22,23]. The PST, PSTF and PSLTF precursor solution was deposited onto a Pt/Ti/$SiO_2$/Si commercial substrate by spin coating at 6000 rpm for 20 s using a spin coater (KW-4B, Chemat Technology) via a syringe filter to avoid particulate contaminations. After spin coating, the films were preheated to 200 °C for 10 min on a hot plate to remove residual water. Then, the films were annealed using a stepwise/successive growth and crystallization engineering method at 400 °C/4 h and 700 °C/2 h in ambient air to remove residual organic components at a heating rate of 5 °C/min, respectively. The film thickness was adjusted by repeating the deposition and the pyrolysis/growth/crystallization cycle. The cross-section micrographs show that the thicknesses of PST, PSTF and PSLTF thin films are 220, 190 and 200 nm, respectively

To check the phase structures of all thin films, X-ray analysis were carried out using a Rigaku MiniFlex600 X-ray diffractometer (XRD, $CuK_\alpha$ radiation, $\lambda = 1.54056$ Å). Surface microstructures and morphology were characterized using atomic force microscope (AFM). A Bruker Dimension ICON was used in these experiments.

A LabRAM HR Evolution micro-Raman spectrometer from Horiba Scientific was used to perform the Raman measurements, while the thin films were maintained at room temperature. The 532 nm line of the Nd:YAG laser beam was focused using a 100x objective, generating an intensity of 0.9 mW at the sample's surface.

To measure the electrical properties, circular Au electrodes were prepared by evaporation through a shadow mask with a $4.9 \times 10^{-2}$ mm$^2$ dot area to obtain an array of capacitors. The deposition was carried out under vacuum ($10^{-6}$ Torr). The dielectric properties and complex impedance analysis of thin films were investigated using Agilent 4294A Precision Impedance Analyzer coupled to a temperature-controlled probe station. The temperature-dependent I-V characteristics were measured using a Keithley 237 source measure unit and a controlled heating stage.

The X-ray photoemission spectra were obtained with a *Scienta Omicron ESCA* + spectrometer system equipped with a *EA 125 hemispherical* analyzer and a *Xm 1000* monochromated x-ray source in *Al kα* (1486.7 eV). The x-ray source was used with a power of 280 W as the spectrometer worked in a constant pass energy mode of 50 eV. In order to compensate the charge effect while obtaining spectra, a *Cn 10 Omicron* Charge neutralizer with a beam energy in 1.6 eV was used. For corrections in peaks shifts due to remaining charge effect, the binding energy of all spectra was scaled using the main peak of *C1s* at 284.5 eV as reference. Wide scan spectra, for peak identification, were recorded with a step of 0.5 eV, while the high-resolution spectra for core levels were obtained using 0.02 eV step.

## 3. Results and discussions

Typical XRD patterns of the samples grown on Si/$SiO_2$/Ti/Pt substrate taken at room temperature are shown in Fig. 1 (panel A). All thin films were found to be polycrystalline with a perovskite phase after calcination at 700 °C. The PST thin films clearly revealed splitting of (0 0 1)/(1 0 0), (1 0 1)/(1 1 0) and (0 0 2)/(2 0 0) peaks, confirming the tetragonal phase, as shown in Fig. 1(a). Nevertheless, for PSTF and PSLTF thin films the splitting of the (0 0 1)/(1 0 0), (1 0 1)/(1 1 0), and (0 0 2)/(2 0 0) peaks was not observed, suggesting a transition from tetragonal to cubic phase. Here the values of lattice parameters a and c were observed to be 0.392 nm and 0.400 nm (PST), 0.392 nm and 0.393 nm (PSTF), 0.392 nm and 0.392 nm (PSLTF). Furthermore, similar decreasing of lattice parameters was observed by Ganegoda et al. [24] Sun et al. [25] in Fe-doped $PbTiO_3$ specimens and by Ye et al. [26] Gong et al. [27] in Fe-doped $Ba_{0.65}Sr_{0.35}TiO_3$ thin films. Raman spectroscopy was carried out to provide additional information to the XRD data, since this method is very sensitive to both variations of local bonding and short- and medium-length range symmetry breaking. Raman spectra of the PST, PSTF and PSLTF thin films are shown in Fig. 1 (panel B). The spectrum of the PST thin films shows the typical signature of a tetragonal perovskite phase, which is also in good agreement with the prototype ferroelectric $PbTiO_3$ [28]. Conversely, PSTF and PSLTF thin films showed spectra less structured due to the co-substitution of Fe and La ions into B-site and A-site sublattice, respectively; this finding clearly suggests a cubic-tetragonal phase transition at room temperature. In particular, for both PSTF and PSLTF thin films, a pronounced Raman active mode at 685 cm$^{-1}$ was observed, caused by the substitution of $Fe^{3+}$ for $Ti^{4+}$. Similar results have been reported in $Sr(Fe_xTi_{1-x})O_{3-\delta}$ samples [29]. In addition, a close inspection of PSTF and PSLTF thin films showed a remarkable persistence of cubic phase Raman peaks, according XRD analysis. The persistence of Raman-active modes is due to the well-known breaking of selection rules induced by an inherent lattice disorder main caused by: (i) presence of intrinsic and extrinsic defects sites, such as oxygen vacancies and cation vacancies, (ii) short and medium-range cationic distortions due to $Fe^{3+}/Ti^{4+}$ or/both $La^{3+}/Sr^{2+}$ substitution. Thus, Raman studies confirmed that both PSTF and PSLTF thin films might be better assigned to a pseudocubic structural phase.

Fig. 1 (panel C) shows the surface morphology of PST, PSTF and PSLTF films deposited on Si/$SiO_2$/Ti/Pt after annealing at 700 °C obtained from atomic force microscopy. All thin films exhibit a rather relatively smooth, precipitates-free and dense surfaces, and spherical-like grains morphologies, indicating the good quality of the thin films. The investigation of the surface topography clearly revealed noticeable differences of the average grain size. The estimated values of grain size and roughness from the AFM images for PST, PSTF and PSLTF thin films on Si/$SiO_2$/Ti/Pt substrate were about 80, 30, and 20 nm, and 7.7, 6.6 and 3.2 nm, respectively.

It is well reported in literature that leakage current properties in ferroelectric thin films can be originated from space charge-limited current (SCLC), Schottky emission, Poole-Frenkel emission, and Fowler-Nordheim tunneling [30–32]. In addition, in Pt/PCT24/Au, Pt/BST/Pt, Pt/SBT/Pt and Pt/PZT/Au capacitors architecture, made with layered perovskite ferroelectric thin films, the main current conduction mechanism is the Schottky emission [33–35]. Therefore, in order to study the current transport mechanism in PST, PSTF and PSLTF thin films, current–voltage characteristics curves were obtained at different temperatures with positive bias voltage applied to the top electrodes and the results are plotted in Fig. 2. A remarkable feature observed in I-V curves was the higher temperature dependence of the leakage current in all the films. All samples exhibited Schottky-related conduction where leakage currents quickly increase with increasing temperature, as clearly revealed by curves in Fig. 2. At higher field region, the current increased exponentially. The metal/PST, PSTF or PSLTF/metal capacitor usually behaves such as a back-to-back Schottky diode. Therefore, conduction mechanism in our thin films should be interpreted in terms of Schottky thermionic emission mechanism which is described by the following equation [34]:

$$J = \left[A^* T^2 \exp\left(\frac{-q(\phi_B - \Delta\phi_B)}{k_B T}\right)\right]\left[\exp\left(\frac{qV}{nk_B T}\right) - 1\right] \quad (1)$$

where V is the applied voltage, T is the absolute temperature, n is the ideality factor, $\Phi_B$ is the Schottky barrier height, $K_B$ is the Boltzmann constant, q is the unit charge, $\Delta\Phi_B$ is the barrier lowering due to electric

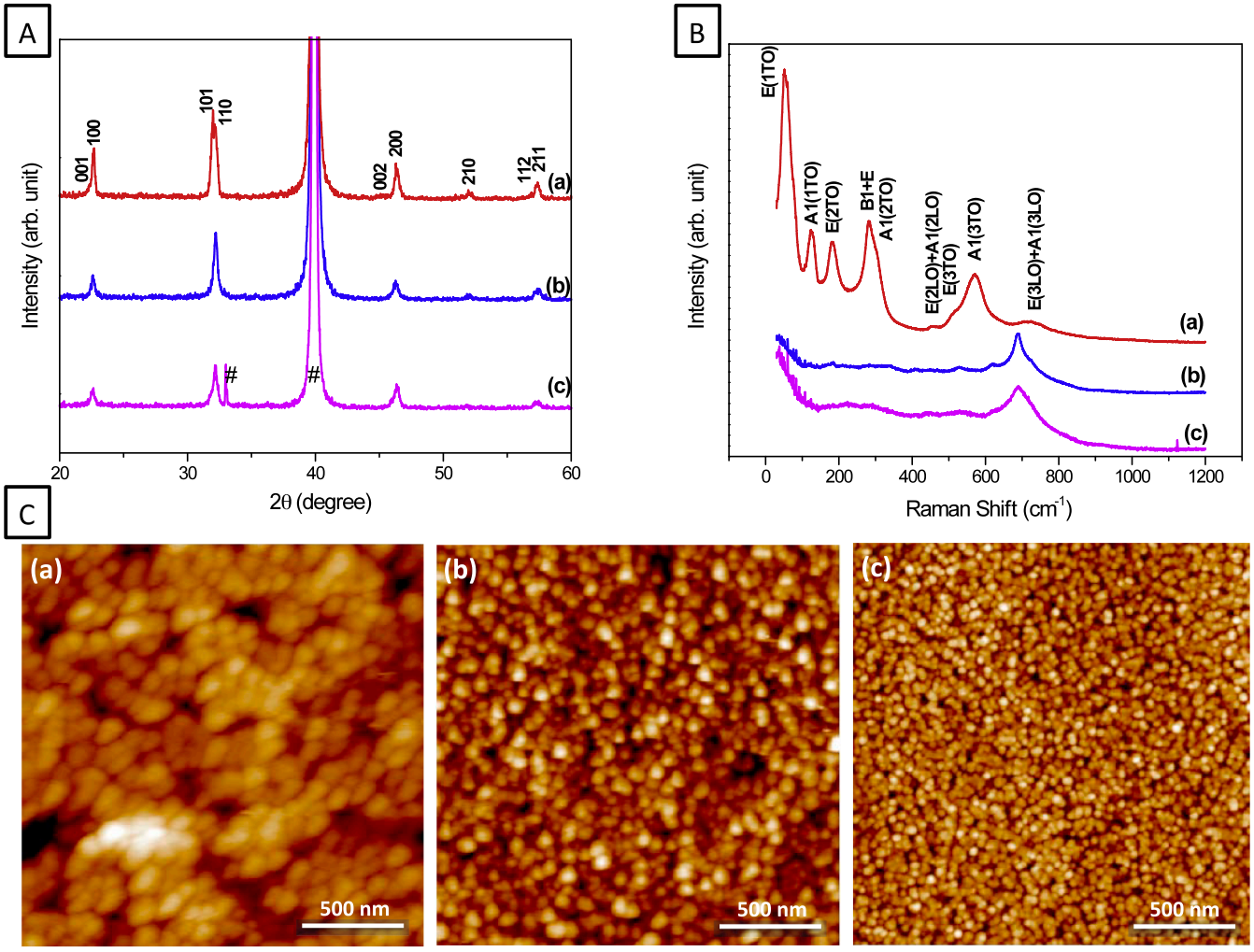


**Fig. 1.** Top panels (A and B) show XRD patterns and Raman spectra of PST (a), PSTF (b) and PSLTF (c) thin films annealed at 700 °C, respectively. Panel (C) depicts AFM images of PST (a), PSTF (b) and PSLTF (c) thin films annealed at 700 °C.

field effect and $A^*$ is known as the Richardson constant, given by [15]

$$A^* = \frac{4\pi e m^* k_B^2}{h^3} \quad (2)$$

Here $m^*$ is the effective electron mass and h is the Planck constant.

As expected from the Schottky theory, the current increases following the increasing temperature: this thermally activated conduction is further enhanced by the applied field. We also have investigated the use of the Poole–Frenkel and space-charge-limited current models, but the fit of the experimental data using these models was quite unreasonable. However, as seen in Fig. 3 the experimental data of $\ln(I_0)$ versus $V^{1/2}$ are extremely well behaved (linear, as expected) over the high voltage region. Additionally, no noticeable changes of the transport mechanism at higher voltages were observed in $Fe^{3+}$, $La^{3+}$ doped PST thin films. This suggested that leakage current is controlled at least by the Schottky thermionic emission in our thin films. There are several ways to extract the Schottky barrier height, but one of the most commonly used is to compare the conduction behavior against temperature. In this sense, in Fig. 4 the variations of $\ln(I_0/T^2)$ versus 1/T were plotted using the I-V data. From these curves the barrier height was estimated, as also shown in Fig. 4, by a least square fitting method and extrapolating it to V = 0. The Schottky barrier heights obtained of the PST, PSTF and PSLTF thin films were found to be 1.20, 0.59 and 0.36 eV, respectively. A similar approach was reported by Gopalan et al. [36]. It was found that the Schottky barrier height decreased when Nb content in Nb-doped $SrTiO_3$ thin films [$SrTi_{1-x}Nb_xO_3$] was increased. Recently, Enriquez et al. [37] reported that the leakage current mechanism in $SrFeO_{3-\delta}$ thin films changed from mainly bulk mediated trap assisted tunneling to interface mediated Schottky emission depending on the oxygen vacancy concentration. In addition, the Schottky conduction mechanism has been reported both for undoped PZT and erbium doped PZT thin films [38]. The barrier height they have found was 0.81 and 0.74 eV, respectively for erbium doped PZT and undoped PZT thin films. Feigl et al. reported a reduction of the Schottky barrier height for PZT thin films doped with Cr acting as acceptor ion [39].

Here, the barrier height was found to decrease with $Fe^{3+}$, $La^{3+}$ co-doping. The increase of positively charged oxygen vacancies migration induced the lowering of the Schotky barrier height (extrinsic defect sites), thus changing the conductive state. It is well known and reported in literature that (i) the intrinsic oxygen vacancies normally occur in the ABO3-δ perovskite-family structure (see Eq. (3)) and (ii) when the doping ion contains a valence lower than that of the ion at the B site, extrinsic oxygen vacancies with positive charge were found to occur to maintain the charge neutrality (see Eq. (4)). Using the Kröger-Vink notation, the above scenario can be represented for the PSTF and PSLTF films as

$$O_O^x \leftrightarrow V_O^{\cdot\cdot} + 2e' + {}^1\!/_2\, O_2(g) \quad (3)$$

$$2Fe_{Ti}^x \leftrightarrow 2Fe_{Ti}' + V_O^{\cdot\cdot} \quad (4)$$

Further, for the PSLTF films the electrical neutrality can be

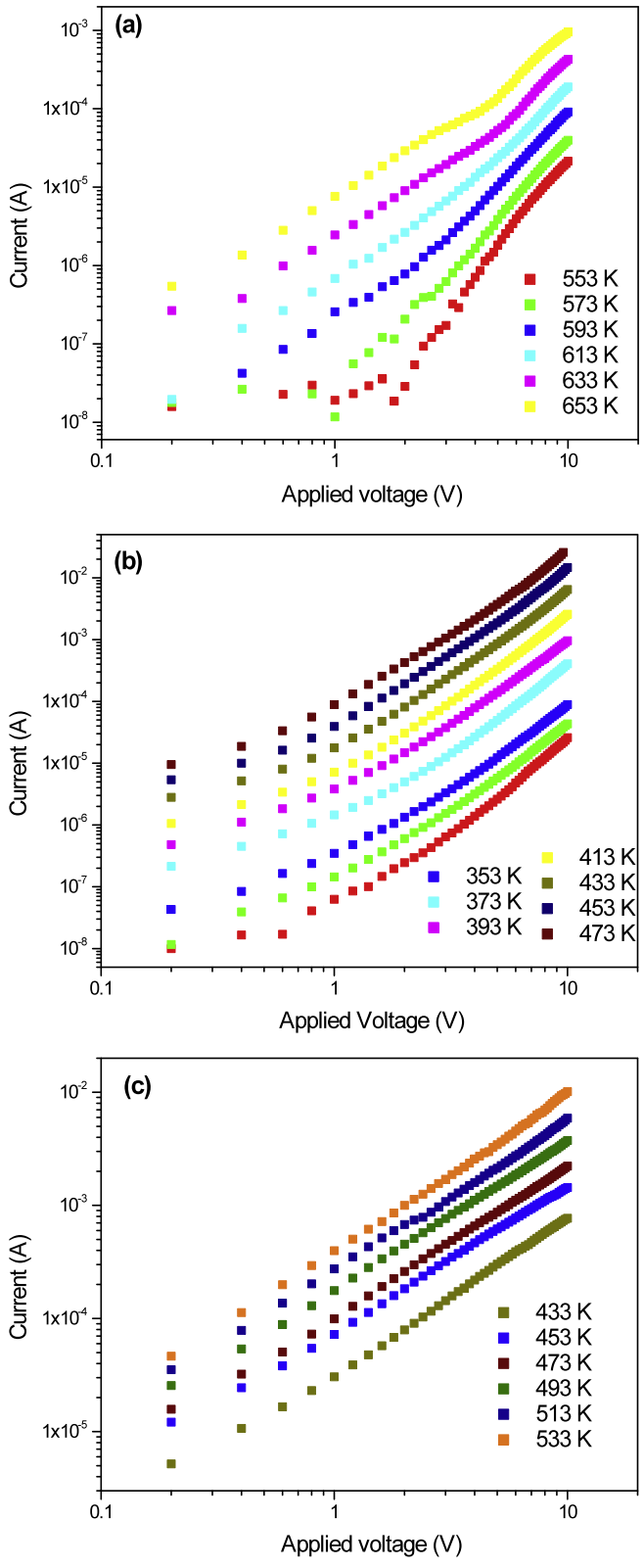


**Fig. 2.** I–V curves obtained at different temperatures for the (a) PST, (b) PSTF and (c) PSLTF thin films.

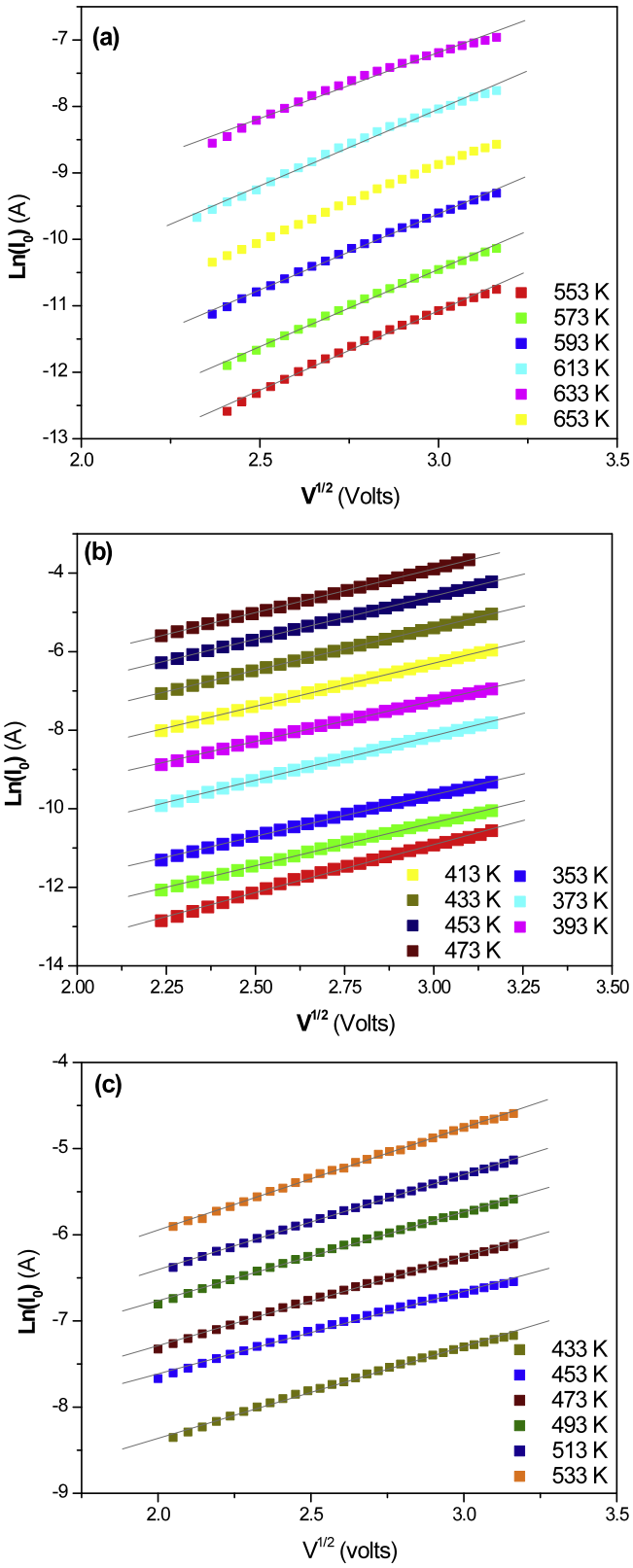


**Fig. 3.** ln(I$_o$) as a function V$^{1/2}$ for the (a) PST, (b) PSTF and (c) PSLTF thin films at different temperatures.

compensated by either oxygen vacancies and/or cation vacancies ($V''_{Sr}$, $V''''_{Ti}$, $V''_{Pb}$) which can also act to create charge traps lowering the Schotkky barrier height. In this scenario different and plausible compensation mechanisms should be considered for explaining PSLTF films behavior. Using Kröger-Vink notation, the charge compensation equations can be represented by

$$Sr_{Sr} \rightarrow La^{\cdot}_{Sr} + e' \quad (5)$$

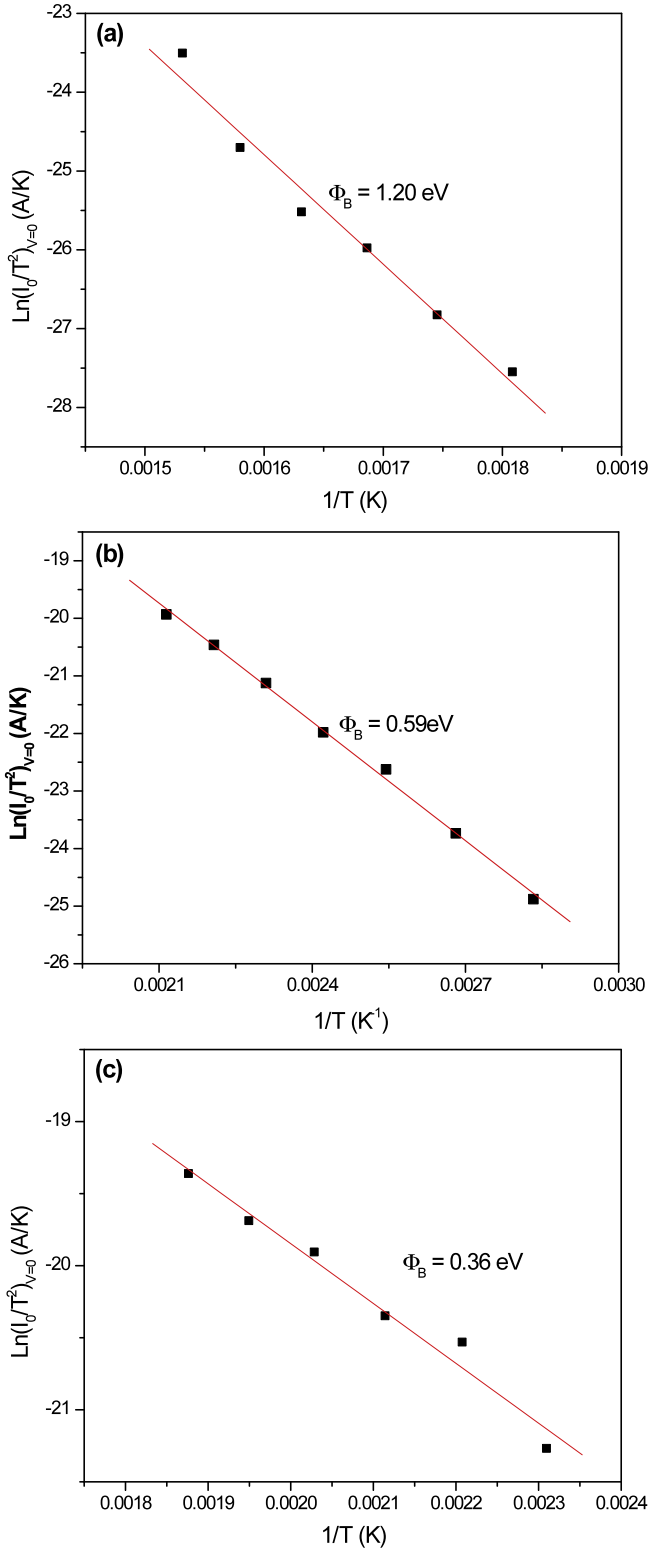


**Fig. 4.** $\ln(I_o/T^2)$ versus 1/T plot for (a) PST, (b) PSTF and (c) PSLTF thin films, from which the Schottky barrier height was estimated.

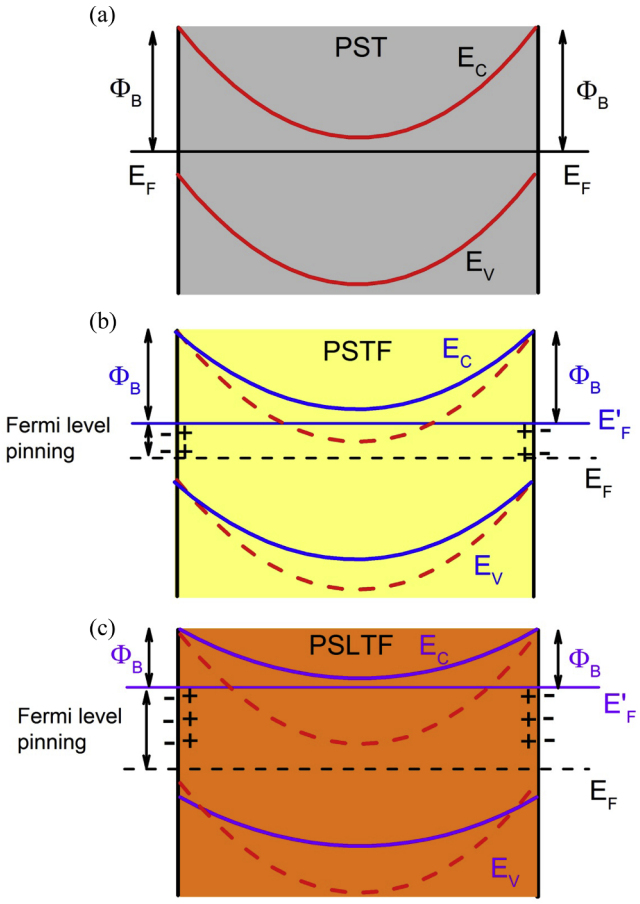


**Fig. 5.** Back-to-back Schottky barriers formation in (a) PST, (b) PSTF and (c) PSLTF thin films. The barrier height decreases as the charges piled up at the films surfaces which in turn pins the Fermi level. Plus and minus signals refer to positive (traps, vacancies) and electrons (metal), respectively; red lines (solid and dashed) refer to PST band edges for comparison. $E_F$ and $E'_F$ are the Fermi levels before and after doping and $\Phi_B$ is the Schottky barrier. (For interpretation of the references to colour in this figure legend, the reader is referred to the web version of this article.)

$$4Sr_{Sr} + Ti_{Ti} \rightarrow 4La_{Sr}^{\cdot} + Vi_{Ti}^{\prime\prime\prime\prime} \quad (6)$$

$$2Fe_{Ti}^{x} \leftrightarrow 2Fe_{Ti}^{\prime} + V_{O}^{\cdot\cdot} \quad (7)$$

$$2La_{Sr}^{x} \rightarrow 2La_{Sr}^{\cdot} + V_{Sr}^{\prime\prime} \quad (8)$$

In fact, for high interface state densities (due to the presence of vacancies, either anions or cations (extrinsic defect sites, Eqs. (3)–(8))) at the surface of films the Fermi level of the films will be affected leading to a lower Schottky barrier height; the Fermi level at the surface is then termed "pinned" by surface states within a narrow range of energy in the bandgap. The energy band diagram of the three different PST (PSTF, PSLTF)/metal capacitor are summarized in Fig. 5.

The Schottky barrier lowering caused by acceptor and donor doping (charge effects) can also be reflected in the impedance spectroscopy data. First, we carried out impedance analysis of $|Z''|$ versus $|Z'|$ over a wide frequency range at room temperature, as seen in Fig. 6. For the PST thin films, the straight line with large slope indicates the film is highly insulating [40]. Conversely, the resulting curves for both acceptor and donor doping PST thin films showed a tendency to form semicircles. This behavior shows that the electrical resistivity for both PSTF and PSLTF thin films decreases indicating that the doping can be effectively controlled in PST films. Therefore, any increase in conduction is expected to be directly related to a decrease in the Schottky barrier height.

In order to have an additional insight into the physical properties of PST, PSTF and PSLTF thin films complex impedance spectra were taken. Fig. 7 shows the variation of the real part of the impedance (Z′) as a function of the frequency at several temperatures for all the thin films. For all temperature scans, PST Z′ component increases until it reaches a particular temperature and then rapidly decreases. This behavior is a signature of the ferroelectric-paraelectric transition which occurs

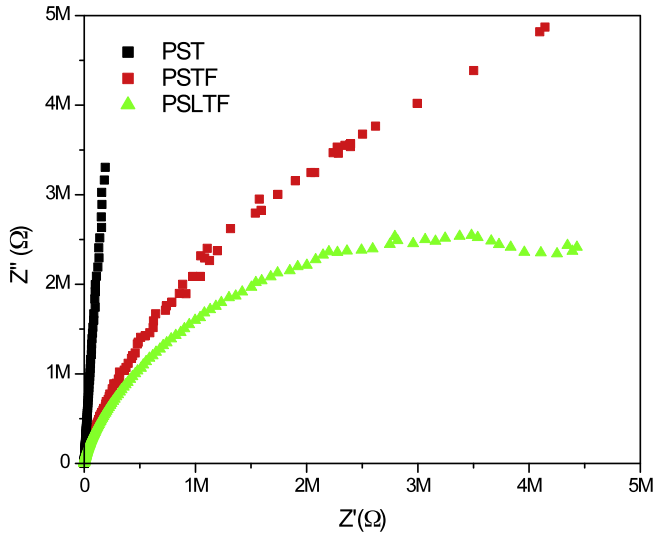


**Fig. 6.** Real and imaginary components of complex impedance at room temperature of PST, PSTF and PSLTF thin films.

approximately at 593 K. These spectra also revealed that the value Z′ falls progressively with increasing temperature and frequency for all thin films. Further, at the low frequency region ($10^2$–$10^4$ Hz), there is a decrease in magnitude of impedance (Z′) when temperature increases showing a negative resistance temperature coefficient (NTCR) behavior [41,42]. In addition, at higher frequencies Z′ values seem to converge independently of the temperature. Such behavior can be related to two reasons, at least: (i) release of the space charges due to the reduction of the barrier heights and (ii) ausence of space charge polarization. The real part (Z′) of the impedance of our thin films is in good agreement with early reported results [43–45]. The frequency dependence of the impedance imaginary part (Z″) (i.e. loss spectrum) at several temperatures is depicted in Fig. 8 for the PST, PSTF and PSLTF thin films. It was found that Z″ versus frequency spectra exhibited relaxation peaks (known as the relaxation frequency). Some features should be highlighted: (i) relaxation stars in well defined temperatures i.e. at 593, 353 and 333 K for thin films PST, PSTF and PSLTF, respectively. This variation indicates the presence of immobile charge carriers at lower temperature for PST thin films. On the contrary, for both PSTF and PSLTF films it indicates the presence of high concentration of mobile charge carriers which are activated at lower temperatures, (ii) a single peak was observed at each temperature and it was further broadened and shifted to higher frequencies following the increase of the temperature. Such behavior suggest the existence of a electrical relaxation phenomena in our thin films; (iii) the loss spectrum seem to converge at higher frequencies due to the absence or release of space charges, and (iv) the magnitude of impedance ($Z''_{max}$) decreases with increasing temperature indicating a decrease in the resistance of the films [46,47].

From the impedance data it was possible to evaluate the relaxation time (τ) using the following relation [42]:

$$\tau = \frac{1}{\omega_{max}} = \frac{1}{2\pi f_{max}} \tag{9}$$

where $f_{max}$ is the relaxation frequency. The dependence of the τ with temperature for all the thin films is shown in Fig. 9. The curves seem to follow the Arrhenius relationship which is given by [42]

$$\tau = \tau_0 \exp\left(\frac{E_a}{k_B T}\right) \tag{10}$$

where $\tau_o$ is a pre-exponential factor, $E_a$ is the activation energy, $k_B$ is the Boltzmann constant and T is the absolute temperature. Activation energies were evaluated from the slope of ln (τ) versus 1/T plot. The activation energy ($E_a$) was estimated to be 1.73, 0.82 and 0.57 eV for

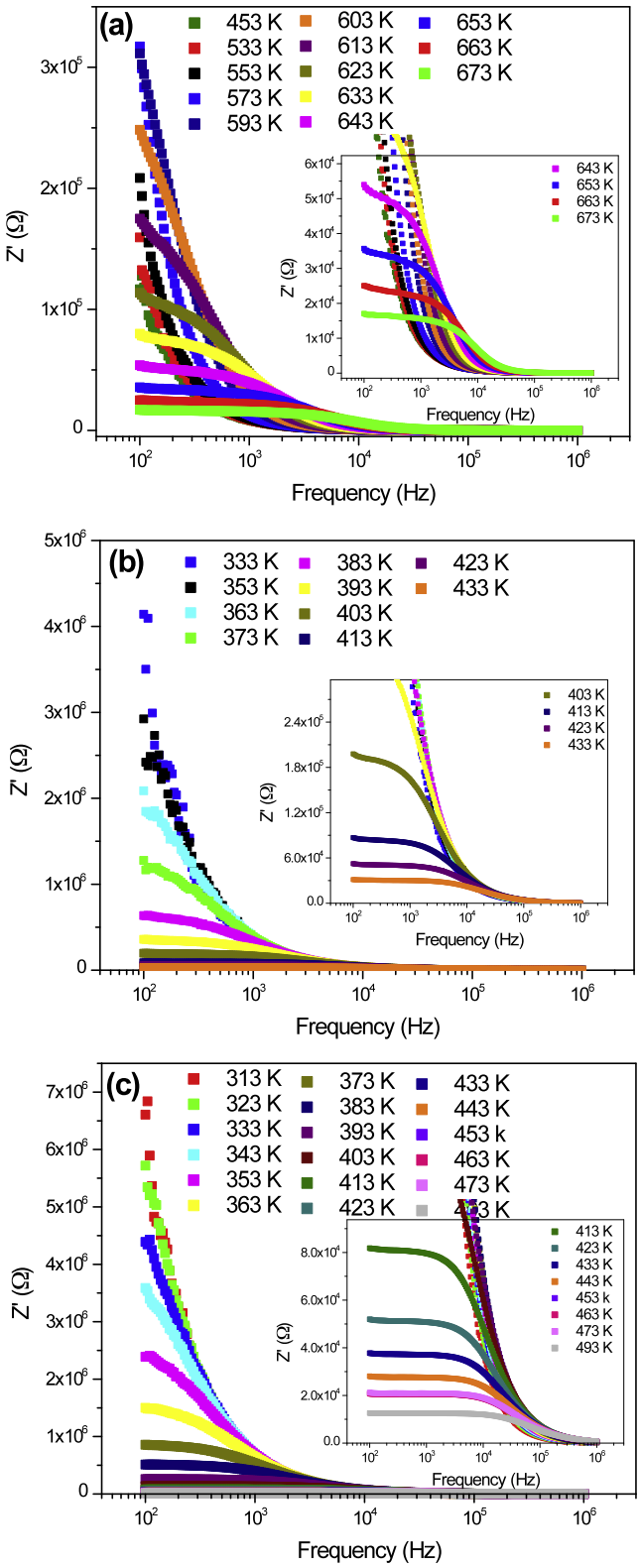


**Fig. 7.** Frequency dependent of the complex impedance real part at selected temperatures for (a) PST, (b) PSTF and (c) PSLTF thin films. Insets (a–c) show enlarged view of the higher temperature and frequencies regions.

PST, PSTF and PSLTF thin films, respectively. Shukla and Choudhary reported a decrease of the activation energy with an increase in Mn concentration for $Pb_{0.92}La_{0.08}Mn_xTi_{1-x}O_3$ compounds [42]. Elbasset et al., observed an activation energy decrease by increasing Sr doping in $Ba_{1-x}Sr_xTiO_3$ samples [48]. In contrast, Zhang et al. have reported an

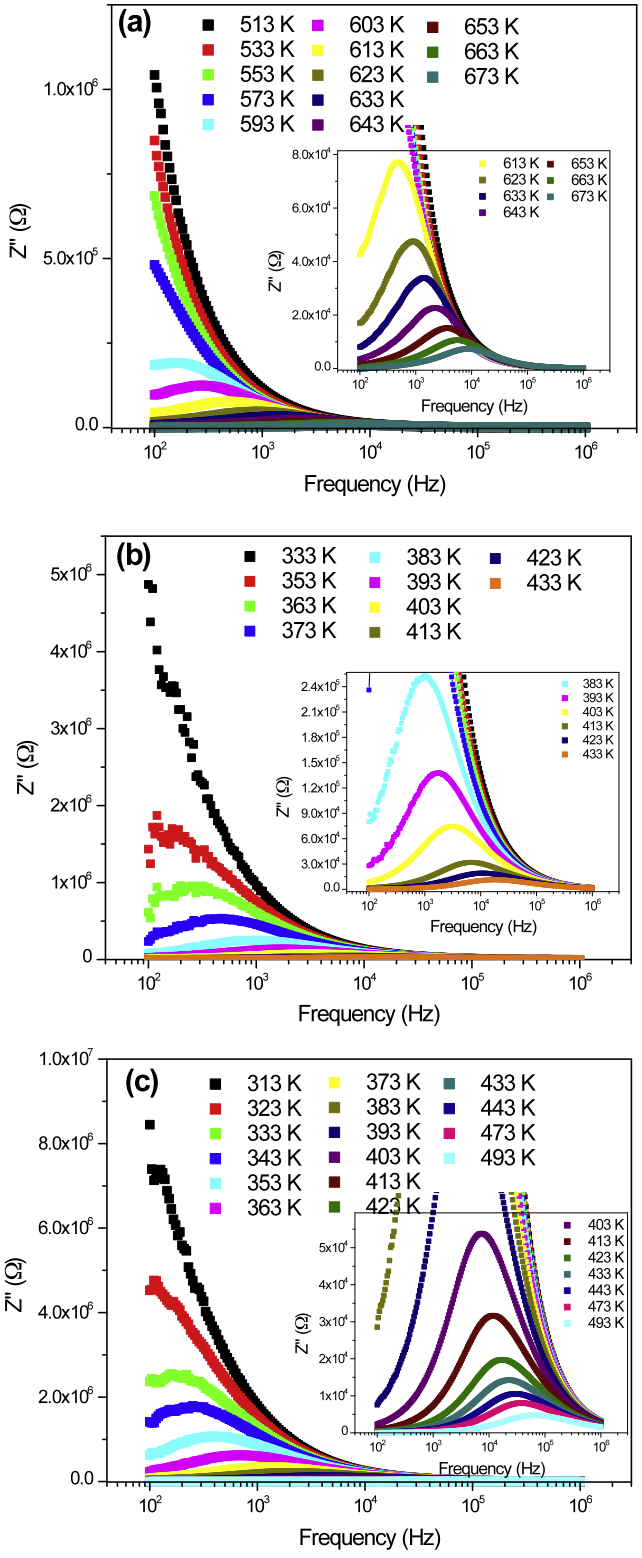


**Fig. 8.** Frequency dependent of the complex impedance imaginary part at selected temperatures for (a) PST, (b) PSTF and (c) PSLTF thin films. Insets (a–c) show enlarged view of the higher temperature and frequencies regions.

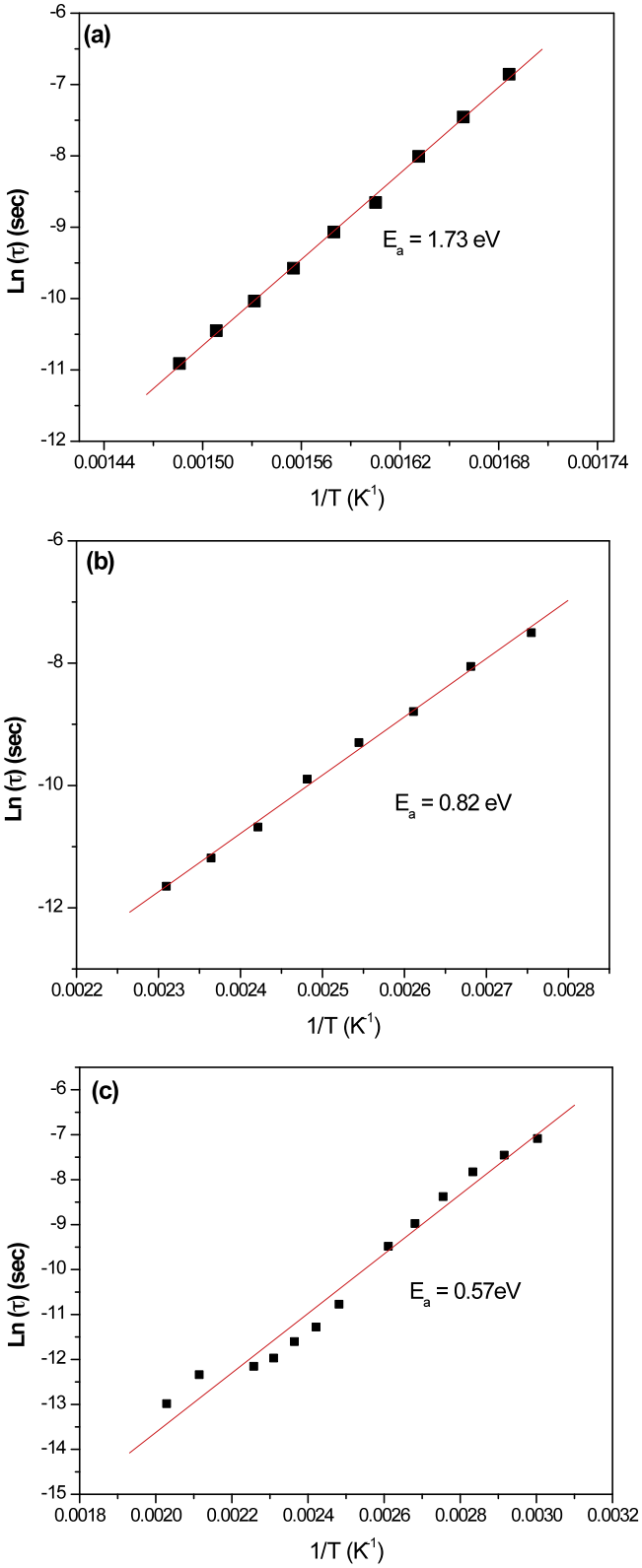


**Fig. 9.** Relaxation time as a function of the reciprocal temperature of (a) PST, (b) PSTF and (c) PSLTF thin films.

increase in $E_a$ related to the suppression or densities lower of oxygen vacancies and vice-versa [49]. The activation energy decreases with increase amounts of $Fe^{3+}$ and $La^{3+}$ co-doping, compared to the PST. This indicates that for both PSTF and PSLTF films have more mobility and higher charge carrier densities than PST films. It is worth noticing that the values of activation energy from our experimental results suggest that oxygen vacancies are the mobile ionic defect species and the responsible for conduction process. Das et al. reported that the activation energy for dielectric relaxation phenomenon of the Ba doped $BiFeO_3$ samples lies between 1.16 and 1.44 eV which was attributed to

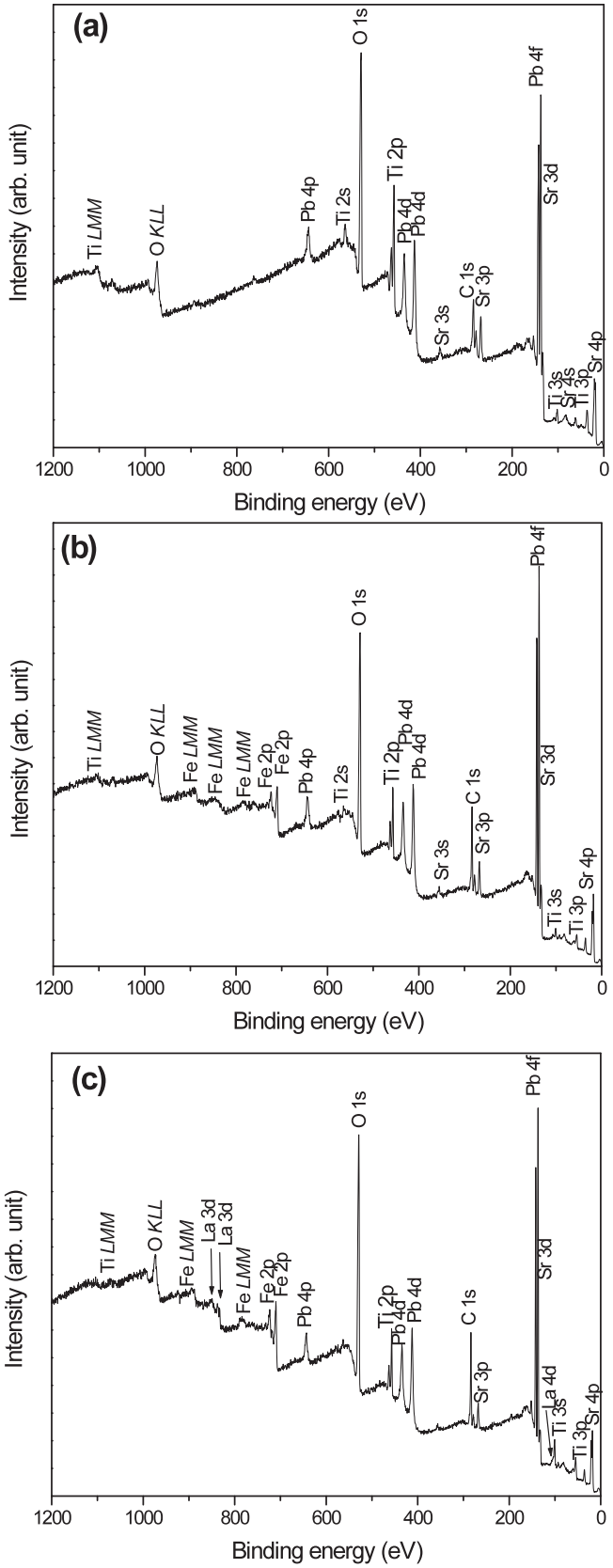


**Fig. 10.** XPS survey scan of (a) PST, (b) PSTF and (c) PSLTF thin films.

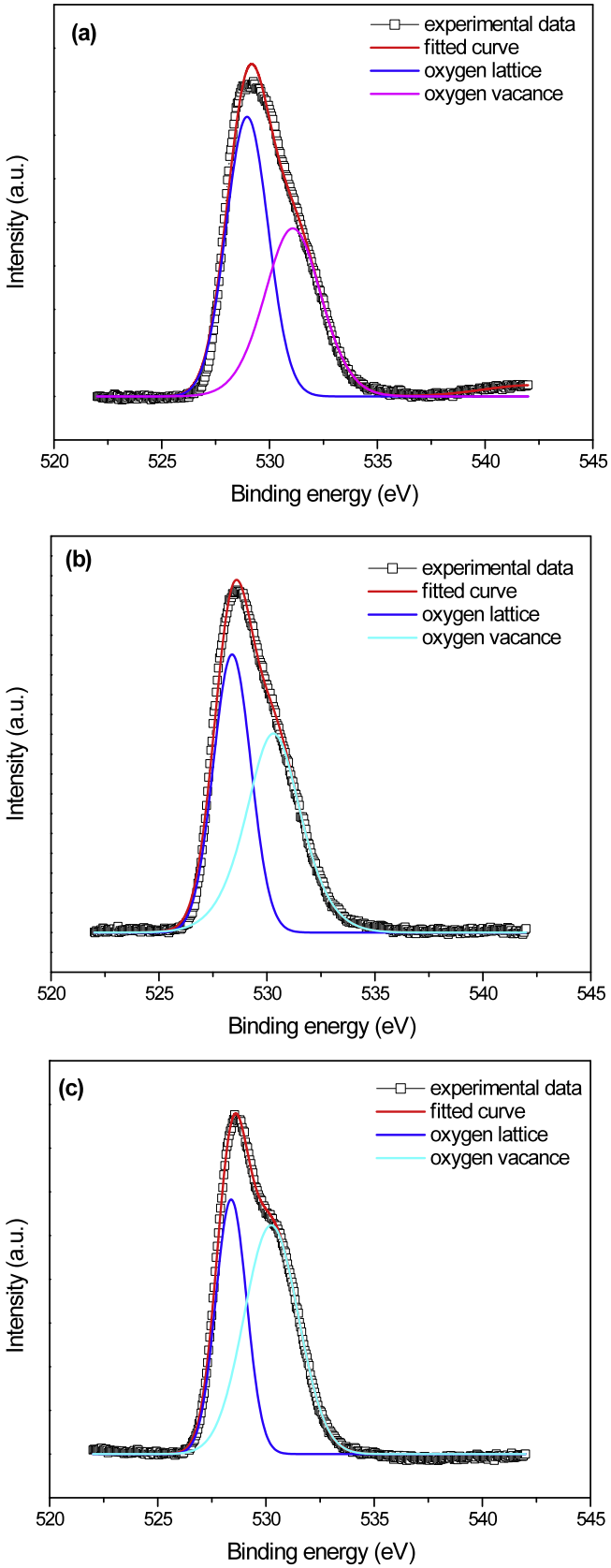


**Fig. 11.** XPS core level spectra of O 1s of (a) PST, (b) PSTF and (c) PSLTF. The O 1s peak is composed of lattice oxygen and oxygen vacancies.

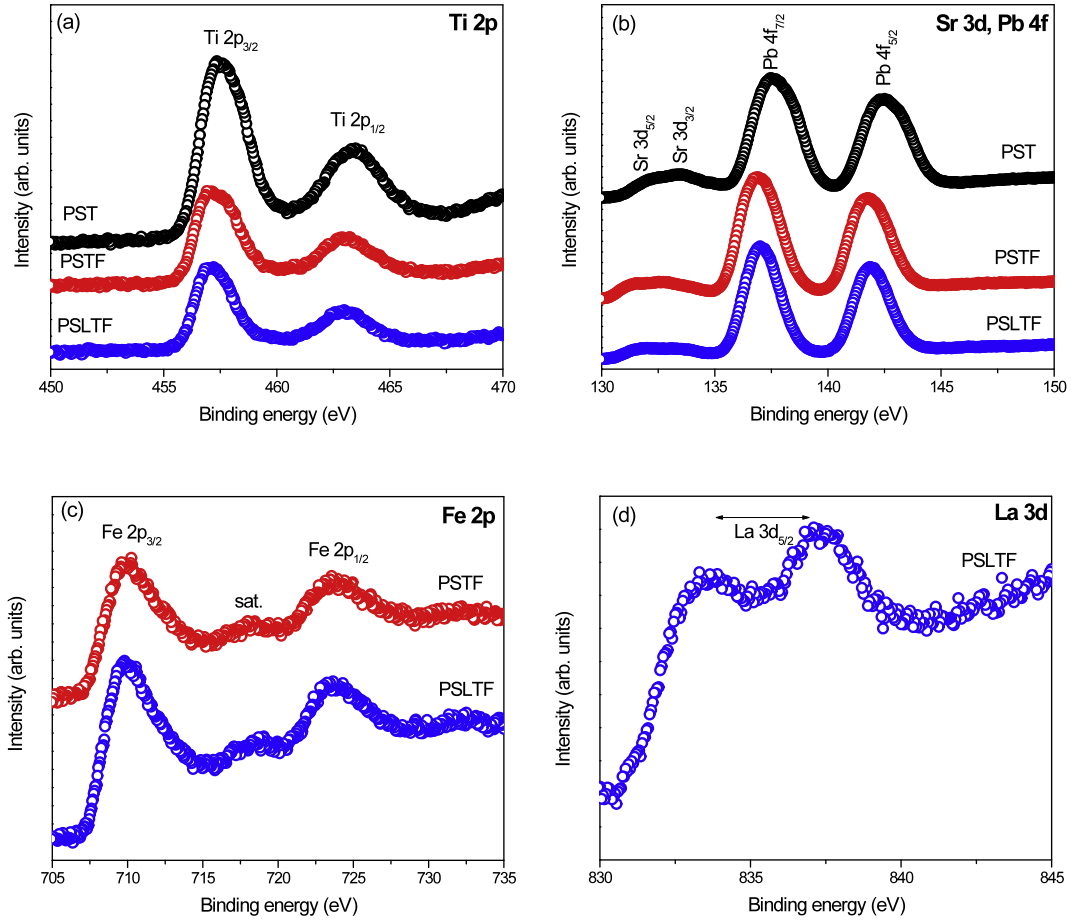


**Fig. 12.** XPS narrow-scan spectra of the (a) Ti 2p, (b) Sr 3d and Pb 4f, (c) Fe 2p, and (d) La 3d binding energy regions for the PST, PSTF and PSLTF thin films.

the presence of oxygen vacancies [50]. It is reasonable, therefore, to assume that our $E_a$ values are in good agreement with those previously reported in literature to the oxygen vacancy diffusion [19,51,52].

Finally, from detailed X-ray photoemission spectra (XPS) analysis the chemical state of each element was studied. Fig. 10 shows XPS survey spectra of PST, STF and PSLTF thin films. The wide scan spectrum of the three samples confirmed the presence of the expected elements [53–56]. In addition, undoped PST films show no $Fe^{3+}$ and $La^{3+}$ signals. Fig. 11 shows the asymmetric O 1s core-level spectra for three thin films which can be fitted by two peaks. The low binding energy peak at ~528.0–528.9 eV was ascribed to the lattice oxygen, whereas high binding energy peak at ~530.0–530.5 eV are normally assigned to the oxygen vacancy defects [50,57,58]. Comparing the O 1s XPS spectra we can unambiguously see a large difference between the three samples: the ratio between the area of the two peaks (low binding energy peak/high binding energy peak) is lower in PSLTF than in PST films, indicating the higher concentration of oxygen vacancies in PSLTF films. Thus it is reasonable assume that the formation of these larger oxygen vacancy defects can be considered as the main responsible by lowering both the Schottky barrier height and the activation energy as confirmed by electrical transport mechanism and complex impedance studies. In addition, Fig. 12 shows the narrow-scan XPS spectra of the Ti 2p, Sr 3d, Pb 4f, Fe 2p, and La 3d peaks. In Fig. 12(a) the PST Ti doublet consists of two peaks related to Ti $2p_{3/2}$ (457.67 eV) and Ti $2p_{1/2}$ (463.26 eV), PSTF Ti $2p_{3/2}$ (457.36 eV) and Ti $2p_{1/2}$ (462.96 eV) and PSLTF Ti $2p_{3/2}$ (457.24 eV) and Ti $2p_{1/2}$ (462.92 eV) corresponding to Ti in its $Ti^{4+}$ valence state [59]. Sr 3d narrow-scan spectra show peaks located at 132.07 and 133.67 eV for PST, at 131.37 eV and 132.87 eV for PSTF, and at 131.77 eV and 133.36 eV for PSLTF that were ascribed to Sr $3d_{5/2}$ and Sr $3d_{3/2}$, respectively, as observed in Fig. 12(b). This indicates that the valence state is $Sr^{2+}$ [60]. The binding energy of Pb $4f_{7/2}$ and Pb $4f_{5/2}$ core level peaks were determined to be 137.67 eV and 142.56 eV for PST, 136.98 eV and 141.86 eV for PSTF, and 137.08 eV and 141.95 eV for PSLTF, corresponding mainly for $Pb^{2+}$, as observed in Fig. 12(b) [61]. Fig. 12(c) shows the narrow-scan spectra of the Fe 2p. The peaks located at 710.06 eV and 723.71 eV for PSTF and at 709.99 eV and 723.67 eV for PSLTF are attribute to Fe $2p_{3/2}$ and Fe $2p_{1/2}$, respectively, which are mainly ascribed to the presence of $Fe^{3+}$ [62]. In addition, Fig. 12(c) exhibits a satellite peak at 718.84 eV sometimes used to determine oxidation state of Fe element, which is in good agreement with many previous reports [62]. The Fig. 12(d) shows that the La 3d doublet consists of two major peaks at 833.31 eV and 837.07 eV for PSLTF, which are attributed to La $3d_{5/2}$, indicating that the $La^{3+}$ valence state of La is present [63].

## 4. Conclusions

We have investigated the electrical transport mechanism and complex impedance behavior of $Fe^{3+}$ and $La^{3+}$ co-substituted PST thin films. Room temperature XRD and Raman spectroscopy analysis revealed the signature of a phase transition from tetragonal to pseudo-cubic in the $Fe^{3+}$ and $La^{3+}$ co-substituted PST films. Temperature-dependent current–voltage characteristics were used to determine the conduction mechanism in these films. For all films Schottky thermionic emission mechanism was found to be the dominant transport mechanism at high voltage. The Schottky barrier heights obtained from the temperature dependence of the I-V curves for the PST, PSTF and PSLTF films were estimated to be 0.74, 0.57, 0.36 eV, respectively. As a result, the Schottky barrier height behavior contributed to the observed leakage current variations. Complex impedance investigation as

function of temperature revealed significant effects in the $Fe^{3+}$ and $La^{3+}$ co-substituted PST films. The Z″ curve shifted towards higher temperatures with increasing frequency, indicating a typical electrical relaxation phenomenon. According to the activation energy values obtained in PST, PSTF and PSLTF films (1.74, 0.87 and 0.57 eV, respectively), the electrical relaxation behavior at the selected temperature region was proposed to be associated to the thermal motion of oxygen vacancies. Besides, the activation energy decreases with $Fe^{3+}$ and $La^{3+}$ doping leading to an enhancement of the conduction characteristics of the samples. In addition, the low $E_a$ value observed in the PSLTF films indicates a larger concentration of oxygen vacancies and vice-versa. These conclusions are supported by X-ray photoelectron spectroscopy measurements.

## Acknowledgments

This study was financially supported by the Brazilian agencies FAPESP and CNPq. In particular, we would like to acknowledge CEPID/CMDMC/INCTMN/CDMF, FAPESP processes no. 11/20536-7, 12/14106-2, and 13/07296-2 and CNPq process no. 470147/2012-1.

## References

[1] H. An, J.Y. Han, B. Kim, J. Song, S.Y. Jeong, C. Franchini, C. Wung, B.S. Lee, Sci. Rep. 6 (2016) 28313.
[2] X. Tang, K. Remmel, X. Lan, J. Deng, H. Xiao, J. Dong, Anal. Chem. 81 (2009) 7844.
[3] A.P. Kulkarni, S. Giddey, S.P.S. Badwal, J. Phys. Chem. 120 (2016) 15675.
[4] Md.S. Sheikh, D. Ghosh, A. Dutta, S. Bhattacharyya, T.P. Sinha, Mat. Sci. Eng. B 226 (2017) 10.
[5] J.P.B. Silva, K. Kamakshi, K.C. Sekhar, J.A. Moreira, A. Almeida, M. Pereira, M.J.M. Gomes, J. Phys. Chem. Sol. 92 (2016) 7.
[6] C. Ang, Z. Yu, L.E. Cross, R. Guo, A.S. Bhalla, Appl. Phys. Lett. 79 (2001) 818.
[7] Y.H. Kim, A. Bhatnagar, E. Pippel, M. Alexe, D. Hesse, J. Appl. Phys. 115 (2014) 043526.
[8] M.C. Hsu, Y.M. Sun, I.C. Leu, M.H. Hon, J. Electroc. Soc. 153 (2006) F260.
[9] D.Y. Wang, N.Y. Chan, R.K. Zheng, C. Kong, D.M. Lin, J.Y. Dai, H.L.W. Chan, S. Li, J. Appl. Phys. 109 (2011) 114105.
[10] P.K. Patel, K.L. Yadav, G. Kaur, RSC Adv. 4 (2014) 28056.
[11] G.W. Leung, M.E. Vickers, T. Fix, M.G. Blamire, J. Phys.: Condens. Matter. 21 (2009) 426003.
[12] H. Wang, L. Liu, J.W. Xu, C.L. Yuan, L. Yang, Bull. Mater. Sci. 36 (2013) 389.
[13] L. Liu, R. Zuo, Q. Sun, Q. Liang, Appl. Surf. Sci. 268 (2013) 327.
[14] A. Kumar, I. Rivera, R.S. Katiyar, J.F. Scott, Appl. Phys. Lett. 92 (2008) 132913.
[15] J. Kolte, A.S. Daryapurkar, M. Agarwal, D.D. Gulwade, P. Gopalan, Thin Solid Films 619 (2016) 308.
[16] I. Coondoo, N. Panwar, R. Vidyasagar, A. Kholkin, Phys. Chem. Chem. Phys. 18 (2016) 31184.
[17] D. Chen, S. Huang, J. Chen, J. Cheng, J. Sol-Gel Sci. Technol. 76 (2015) 220.
[18] W. Li, W. Zhang, L. Wang, J. Gu, A. Chen, R. Zhao, Y. Liang, H. Guo, R. Tang, C. Wang, K. Jin, H. Wang, H. Yang, Sci. Rep. 5 (2015) 11335.
[19] Q. Ke, X. Lou, Y. Wang, J. Wang, Phys. Rev. B 82 (2010) 024102.
[20] A. Lahmar, S. Habouti, C.H. Solterbeck, M. Es-Souni, B. Elouadi, J. Appl. Phys. 105 (2009) 014111.
[21] W.L. Zhang, M.H. Tang, Y. Xiong, S.A. Yan, C.P. Cheng, G. Li, Y.G. Xiao, Z. Li, RSC Adv. 7 (2017) 20929.
[22] F.M. Pontes, D.S.L. Pontes, A.J. Chiquito, Marcelo A. Pereira-da-Silva, E. Longo, Mat. Lett. 138 (2015) 179.
[23] F.M. Pontes, A.J. Chiquito, W.B. Bastos, Marcelo A. Pereira-da-Silva, E. Longo, J. Mat. Chem. C 4 (2016) 9331.
[24] H. Ganegoda, J.A. Kaduk, C.U. Segre, Powder Diffr. 28 (2013) 254.
[25] C. Sun, J. Wang, H. Kang, J. Chen, M.J. Kim, X. Xing, Dalton Trans. 39 (2010) 9952.
[26] Y. Ye, T. Guo, Ceram. Inter. 35 (2009) 2761.
[27] J. Gong, J. Cheng, W. Zhu, S. Yu, W. Wu, M. Zhongyan, IEEE Trans. Ultrason., Ferroelectr., Frequency Control 54 (2007) 2579.
[28] M. Imada, A. Fujimori, Y. Tokura, Rev. Mod. Phys. 70 (1998) 1039.
[29] M. Vračar, A. Kuzmin, R. Merkle, J. Purans, E.A. Kotomin, J. Maier, O. Mathon, Phys. Rev. B 76 (2007) 174107.
[30] R.T. Tung, Appl. Phys. Rev. 1 (2014) 011304.
[31] E.W. Lim, R. Ismail, Electronics 4 (2015) 586.
[32] D.Y. Wang, D.M. Lin, K.W. Kwok, N.Y. Chan, J.Y. Dai, S. Li, H.L.W. Chan, Appl. Phys. Lett. 98 (2011) 022902.
[33] J.T. Pi-Chun, C. Si-min, L.J. Ya-min, J. Appl. Phys. 95 (2004) 3120.
[34] F.M. Pontes, D.S.L. Pontes, E.R. Leite, E. Longo, A.J. Chiquito, P.S. Pizani, J.A. Varela, J. Appl. Phys. 94 (2003) 7256.
[35] R.R. Das, P. Bhattacharya, R.S. Katiyar, A.S. Bhalla, J. Appl. Phys. 92 (2002) 6160.
[36] S. Gopalan, V. Balu, J.H. Lee, J. Hee-Han, J.C. Lee, Appl. Phys. Lett. 77 (2000) 1526.
[37] E. Enriquez, A. Chen, Z. Harrell, P. Dowden, N. Koskelo, J. Roback, M. Janoschek, C. Chen, Q. Jia, Sci. Rep. 7 (2017) 46184.
[38] M. Es-Souni, N. Zhang, S. Iakovlev, C.H. Solterbeck, A. Piorra, Thin Solid Films 440 (2003) 26.
[39] L. Feigl, E. Pippel, L. Pintilie, M. Alexe, D. Hesse, J. Appl. Phys. 105 (2009) 126103.
[40] J.R. Mac Donald, Impedance Spectroscopy, John Wiley and Sons, New York, 1987.
[41] M.K. Adak, A. Mukherjee, A. Chowdhury, J. Khatun, U.K. Ghorai, D. Dhak, J. Mater. Sci.: Mater. Electron. 29 (2018) 15847.
[42] M.K. Adak, A. Mukherjee, A. Chowdhury, U.K. Ghorai, D. Dhak, J. Alloy. Compd. 740 (2018) 203.
[43] A. Laha, S.B. Krupanidhi, Mater. Sci. Eng., B 98 (2003) 204.
[44] M.R. Biswal, J. Nanda, N.C. Mishra, S. Anwar, A. Mishra, Adv. Mat. Lett. 5 (2014) 531.
[45] A. Selmi, O. Khaldi, M. Mascot, F. Jomni, J.C. Carru, J. Mater. Sci.: Mater. Electron. 27 (2016) 11299.
[46] D.K. Pradhan, R.N.P. Chowdhury, T.K. Nath, Appl. Nanosci. 2 (2012) 261.
[47] S. Hcini, A. Selmi, H. Rahmouni, A. Omri, M.L. Bouazizi, Ceram. Int. 43 (2017) 2529.
[48] A. Elbasset, S. Sayouri, F. Abdi, T. Lamcharfi, L. Mrharrab, Mater. Sci. Eng. 186 (2017) 012018.
[49] M.F. Zhang, Y. Wang, K.F. Wang, J.S. Zhu, J.-M. Liu, J. Appl. Phys. 105 (2009) 061639.
[50] R. Das, S. Sharma, K. Mandal, J. Magn. Magn. Mater. 401 (2016) 129.
[51] Y. Wang, Y. Pu, P. Zhang, J. Alloy. Compd. 653 (2015) 596.
[52] S.K. Rout, A. Hussian, J.S. Lee, I.W. Kim, S.I. Woo, J. Alloy. Compd. 477 (2009) 706.
[53] Y. Shuai, S. Zhou, D. Burger, H. Reuther, I. Skorupa, V. John, M. Helm, H. Schmidt, J. Appl. Phys. 109 (2011) 084105.
[54] M. Es-Souni, E. Girdauskaite, S. Iakovlev, C.-H. Solterbeck, J. Appl. Phys. 96 (2004) 5691.
[55] Y.P. Jiang, X.G. Tang, Y.C. Zhou, Q.X. Liu, Prog. Nat. Sci-Mater. 21 (2011) 198.
[56] Z. Quan, H. Hu, S. Xu, W. Liu, G. Fang, M. Li, X. Zhao, J. Sol-Gel Sci. Technol. 48 (2008) 261.
[57] D. Pang, Z. Yi, RSC Adv. 7 (2017) 19448.
[58] S. Fuentes, P. Munoz, N. Barraza, E. Chavez-Angel, C.M. Sotomayor Torres, J. Sol-Gel Sci. Technol. 75 (2015) 593.
[59] Z. Pan, J. Chen, X. Jiang, Z. Lin, L. Zhang, L. Fan, Y. Rong, L. Hu, H. Liu, Y. Ren, X. Kuang, X. Xing, Inorg. Chem. 56 (2017) 2589.
[60] S. Fuentes, P. Munoz, N. Barraza, E. Chavez-Angel, C.M.S. Torres, J. Sol-Gel Sci. Technol. 75 (2015) 593.
[61] H. Borkar, V. Rao, M. Tomar, V. Gupta, J.F. Scott, A. Kumar, RSC Adv. 7 (2017) 12842.
[62] C.D. Pham, J. Chang, M.A. Zurbuchen, J.P. Chang, Chem. Mater. 27 (2015) 7282.
[63] S. Mickevicius, S. Grebinskij, V. Bondarenka, B. Vengalis, K. Sliuziene, B.A. Orlowski, V. Osinniy, W. Drube, J. Alloy. Compd. 423 (2006) 107.